**Accelerated Ionic Motion in Amorphous Memristor Oxides for Non-Volatile Memories and Neuromorphic Computing**

*Rafael Schmitt, Markus Kubicek, Eva Sediva, Morgan Trassin, Mads C. Weber, Antonella Rossi, Herbert Hutter, Jens Kreisel, Manfred Fiebig, Jennifer L.M. Rupp\**

Dr. Rafael Schmitt, Dr. Markus Kubicek, Eva Sediva, Prof. Jennifer L.M. Rupp
Electrochemical Materials, Department of Materials, ETH Zürich, Hönggerbergring 64, 8093 Zürich, Switzerland
jrupp@mit.edu

Dr. Markus Kubicek, Prof. Herbert Hutter
Institute of Chemical Technologies and Analytics, Technische Universität Wien, Getreidemarkt 9/164EC, 1060 Vienna, Austria

Eva Sediva, Prof. Jennifer L.M. Rupp
Electrochemical Materials, Department of Materials Science and Engineering, Massachusetts Institute of Technology, 77 Massachusetts Ave, 8-242, Cambridge, MA, 02139, USA

Dr. Morgan Trassin, Dr. Mads C. Weber, Prof. Manfred Fiebig
Multifunctional Ferroic Materials, Department of Materials, ETH Zurich, Vladimir-Prelog-Weg 1-5/10, 8093 Zürich, Switzerland

Dr. Mads C. Weber, Prof. Jens Kreisel

Materials Research and Technology Department, Luxembourg Institute of Science and Technology, 5, Avenue des Hauts-Fourneaux, 4362 Esch-sur-Alzette, Luxembourg

Physics and Materials Science Research Unit, University of Luxembourg, 41 Rue du Brill, 4422 Belvaux, Luxembourg


Prof. Antonella Rossi

Dipartimento di Scienze Chimiche e Geologiche, Università di Cagliari, Via Università 40, 9124 Cagliari Italy

Laboratory for Surface Science and Technology, Department of Materials, ETH Zurich, Vladimir-Prelog-Weg 5, 8093 Zurich, Switzerland


Prof. Jennifer L.M. Rupp

Electrochemical Materials, Department of Electrical Engineering and Computer Science, Massachusetts Institute of Technology, 77 Massachusetts Ave, 8-242, Cambridge, MA, 02139, USA

Memristive devices based on mixed ionic-electronic resistive switches have an enormous potential to replace today's transistor-based memories and Von Neumann computing architectures thanks to their ability for non-volatile information storage and neuromorphic computing. It remains still unclear however how oxide films in amorphous state propagate their ionic carriers at high local electric fields. By using memristive model devices based on $LaFeO_3$ with either amorphous or epitaxial nanostructures, we engineer the structural local bonding units and increase the oxygen ionic diffusion coefficient by one order of magnitude for the amorphous oxide, affecting the resistive switching operation. We show that only devices based on amorphous $LaFeO_3$ films reveal memristive behavior due to their increased oxygen vacancy concentration. We achieved stable resistive switching with switching times down to microseconds and confirm that it is predominantly the oxygen ionic diffusion character and not electronic defect state changes that modulate the resistive switching device response. Ultimately, these results show that the local arrangement of structural bonding units in amorphous perovskite films at room temperature can be used to largely tune the oxygen vacancy (defect) kinetics for resistive switches (memristors) that are both theoretically challenging to predict and promising for future memory and neuromorphic computing applications.
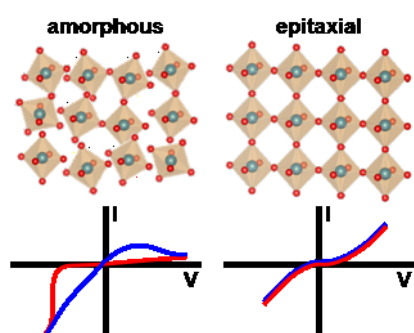
**Introduction**

The continuous quest for enlarged memory storage density is driven by the downscaling of standard silicon-based memory technologies. The miniaturization of the node sizes soon reaches the physical limits in terms of size and power dissipation and requires new computing technologies to overcome these limits.[1, 2] Solutions, where information processing and storage are on the same physical platform, are alternatives to classic Von Neumann computing architectures.[3] Here, novel memory and computing architectures based on resistive switching devices are promising building blocks for future electronics. Resistive switches are one of the few emerging memory technologies besides magnetic and ferroelectric random access memories that satisfy the switching speed requirements in addition to non-volatility.[4] The time-scale non-linearity of sub-nanosecond switching and years of storage is guaranteed by the unique electrochemical processes, whose details are still under investigation. Furthermore, the low power consumption and the multi-level memory operation makes resistive switching devices interesting circuit elements for neuromorphic computing.[5]

In general, electrochemical memristive devices are characterized by a pinched hysteretic current-voltage response when subjected to a bipolar periodic signal.[6] The various resistance states can be addressed upon polarity change of the bias signal on the *electrode/oxide/electrode* structures and altered by the flux of the charge carriers, namely oxygen ions and electronic carriers, passed through the device.[7, 8] On an atomistic scale, the resistive switching in metal-oxide-based devices is mostly driven by valence changes in the oxide counter-balancing the variations in the oxygen anionic defect concentration, and configuration profiles to maintain charge neutrality.[9] Even though resistive switching has been reported for many different binary oxides and perovskites,[10] only very recently first attempts to alter oxygen-vacancy defects and their states by systematic extrinsic doping have

been presented.[9] The use of amorphous oxides as memristor constituent is elegant as they can be processed at lower temperatures compared to polycrystalline oxides to allow easy CMOS integration and cost reduction during the production of hardware components. Nevertheless, most studies on the investigation of the switching mechanism are made on crystalline or epitaxial switching oxides and to date it is unclear how this knowledge can be used for the design of devices with amorphous microstructure.

**Amorphous to Epitaxial Memristor Oxides: Defect Propagation at High Fields**

Resistive switching is observed in different microstructures such as single crystals,[11, 12] epitaxial,[13, 14, 15] polycrystalline,[16, 17] or amorphous films,[18, 19, 20] on the example of $SrTiO_3$. The defect density in the switching oxide differs strongly depending on the thin film microstructure; amorphous films exhibit a very high number of defects, while epitaxially grown films show no grain boundaries and a low number of structural defects. It is known that the microstructure and crystallinity strongly influence the electrical,[21, 22, 23, 24] as well as the ionic [25, 26] conductivity of oxides as it implicates the mobility of charge carriers. Also, it was shown that the ionic motion can be varied depending on the local bonding unit arrangements in amorphous garnets,[27] and this requires the understanding of the structure and chemical bonding in amorphous perovskites.[28] Comparing the oxygen-vacancy diffusion coefficients in amorphous and polycrystalline microstructures determined with the memristor-based Cottrell analysis reveals a slightly higher diffusion coefficient in the defectuous amorphous memristors (*i.e.* $5\times10^{-11}$ $cm^2s^{-1}$ (amorphous) *vs.* $3\times10^{-11}$ $cm^2s^{-1}$ (polycrystalline) for a similar electric field of $3\times10^6$ $Vm^{-1}$) but remains in a comparable order of magnitude.[19, 29] It is therefore of great importance to understand how amorphous oxides conduct, in particular when

operated at ambient and at high electric fields such as in memristors and how they compare to epitaxial oxides in their memristive properties. This will allow a better understanding of the mechanism in view of materials engineering, and it is also an important base for future computational work.[25, 26, 30] A body of work gives evidence of the importance of investigating the microstructure of memristive oxides by switching individual dislocations,[12] altering the defect distribution,[31] the crystallinity,[32] or the post-crystallization of amorphous films[33] on the examples of $SrTiO_3$, $Sr_2TiO_4$, $La_{0.7}Ca_{0.3}MnO_3$, and $HfO_2$. Despite the processing knowledge, such studies have not been extended to memristive model structures ranging from amorphous to epitaxial films yet. Model studies comparing amorphous and crystalline films are important to understand the role of concentration and mobility of defects for such oxides and switching structures under high electric fields.

**Perovskite Memristor Constituents**

In this study we selected $LaFeO_3$ as material system to vary the defect density in the memristor oxide. Lanthanum-based perovskites are well-investigated mixed ionic-electronic conductors that undergo redox reactions, which make them interesting candidates for resistive switching applications,[34, 35] as also reported in a recent review by Burriel and co-workers.[36] $LaFeO_3$ is a mixed oxygen anionic-electronic conducting oxide with well-described defect models and conduction mechanisms,[37, 38] and band structure[39] with mainly p-type conductivity in air.[38] $LaFeO_3$ is significant for various application fields such as solar-to-fuel conversion for renewable syngas synthesis,[40, 41] cathode material for solid oxide fuel cells,[42] catalysts for methane combustion,[43] or gas sensors.[44] Memristors showing resistive switching based on crystalline $LaFeO_3$ oxides have been

reported by Sawa group, integrated as part of an oxide bilayer in combination with BiFeO$_3$,[45, 46] or by Xue group in a solid solution with PbTiO$_3$.[47, 48] To the best of our knowledge, single films of LaFeO$_3$ have neither been processed as memristor constituent material nor have these been investigated regarding their resistive switching behavior.

In conclusion, amorphous structures have an enormous potential for memristive devices, but it is unclear how they compare to epitaxial devices with low structural defect concentrations. Through this work, we provide amorphous LaFeO$_3$ memristors and compare the resistive switching, short range order and oxidation states to epitaxially grown low-defect LaFeO$_3$ memristors. By our model experiment, we show the high defect density variation for 20 nm LaFeO$_3$ thin films and demonstrate their necessity for reliable operation in amorphous memristive devices. Ultimately, the knowledge provided here contributes to the efforts to understand how structural defect engineering in oxide thin-film components can be used for the design of future switching oxide memristive memories and neuromorphic computing architectures.

**Results and Discussion**

Defect-engineered LaFeO$_3$ Resistive Switching Devices: Amorphous vs. Epitaxial Oxide Architectures

We take advantage of the flexibility of thin-film growth to design resistive switching model structures, where the switching LaFeO$_3$ constituent is either deposited as an *amorphous (high number of defects)* or *epitaxially grown single crystalline* film *(low number of defects, no grain boundaries)*. The structure in the "amorphous" LaFeO$_3$ device can be more precisely described as X−ray amorphous with a local order but we will simply refer to it as amorphous. For each of these resistive switching devices, the active LaFeO$_3$ film is sandwiched between a thin epitaxially grown LaNiO$_3$ bottom electrode and a platinum top electrode onto a single crystalline LaAlO$_3$ substrate of (001) orientation, **Figure 1**a. The size of the platinum top electrodes is varied between 40 to 320 μm in diameter as shown in the optical micrograph, **Figure 1**b. The defect density of the active oxide layer can be tuned by varying the pulsed laser deposition (PLD) temperature from 500°C to 700°C keeping the total film thickness fixed at 20 nm for the LaFeO$_3$ oxide. We begin by examining the relationship between microstructure and deposition conditions for the LaFeO$_3$ constituent of the two model resistive switches. **Figure 1**c-d show the surface topography measured by atomic force microscopy (AFM) The topography of the LaFeO$_3$ grown at moderate deposition temperatures of 500°C reveals a flat surface of 0.75 nm roughness, **Figure 1**c. The surface roughness of LaFeO$_3$ grown at 700°C decreases to 0.21 nm, and unit cell steps originating from the substrate miscut are resolved in the topography measurements, revealing an atomically flat film, **Figure 1**d. High-resolution transmission electron micrographs (HR-TEM) of the device cross-section reveal the microstructures of the memristor devices displaying the thin LaFeO$_3$ film constituents, bottom LaNiO$_3$ and top Pt electrodes and the substrate of LaAlO$_3$, **Figure 1**e-f. Both model microstructures have in common

that no grain boundaries are visible for the 20-nm-thick memristive oxide $LaFeO_3$ over the length of the focused ion beam (FIB)-cut TEM-lamella, and $LaNiO_3$ is grown equally resulting in 5 nm-thin epitaxial films with a sheet resistance below 1 kΩ. The $LaFeO_3$ film deposited at 500°C shows no crystalline order, **Figure 1**e, while the film deposited at 700°C reveals epitaxial film growth, **Figure 1**f. The processing temperature of the amorphous layers is chosen above the typical CMOS-compatible processing temperatures of 450°C to ensure that the morphology would withstand the temperatures at the final CMOS-processing steps. However, one can engineer amorphous films in various ways and has overall a wide range to manipulate the amorphous state from low to medium temperature (room temperature to 500°C).

The absence of preferential orientations in the spherical shape of the diffraction pattern for the low-temperature-deposited film confirms an amorphous microstructure while the diffraction pattern of the high-temperature deposited film demonstrates the cubic structure of the $LaFeO_3$ film. The X–ray diffraction (XRD) results are presented in Supporting Information S1 and show the distinct pattern of epitaxial $LaFeO_3$ for the high-temperature deposition, and no peak for the amorphous oxide deposited at low temperature. We confirm that $LaFeO_3$ is successfully grown in two microstructure types for the memristive devices, being with clear, ordered atoms for the $LaFeO_3$ indicating epitaxial growth (high-temperature deposition) and without any long-range order for the amorphous memristor (low-temperature deposition). We further confirm that there is no intermixing of cations at the perovskite interfaces of electrolyte-electrode measurable by energy dispersive X–ray spectroscopy (EDXS) for the memristor devices irrespective of growth temperature, see Supporting Information S2.

Next, we carry out memristor performance tests of the devices to understand the implication of charge and mass transport for amorphous and epitaxial LaFeO$_3$-structures. The role of structural defects on memristance is investigated by cyclic voltammetry and is further compared to the electrochemical impedance responses of the LaFeO$_3$ model memristive devices, see **Figure 2**. Here, the kinetics of the SET process of the amorphous devices are further accessed by the voltage pulse experiments and write and read processes are emulated to demonstrate a proof-of-concept for a memristive computer memory.

Nonlinear Switching Dynamics for Defect Modulated LaFeO$_3$ Devices

We turn to the current-voltage characteristics of pristine memristive devices and compare the memristive devices with amorphous and epitaxial LaFeO$_3$-constituents.

*Amorphous memristors:* For the amorphous LaFeO$_3$-based memristive switches, we observe stable and hysteretic *I-V* resistive switching profiles for over 50 consecutive cycles, **Figure 2**a. No electroforming is required in the device to induce the switching. For positive bias on the Pt top electrode, the resistance of the device increases gradually, switching the memory into the high-resistance OFF-state starting at a RESET voltage of 1 V, **Figure 2**a. Reversing the polarity to a SET voltage of −4 V switches the device back into the low-resistance ON-state leading to a sudden current increase of one order of magnitude. Two distinct resistance states can be defined at the origin: namely, the high-resistance OFF-state and the low-resistance ON-state with an average $R_{OFF}/R_{ON}$ ratio of up to 100 over the 50 cycles tested. Studying the resistive switching properties of the amorphous LaFeO$_3$ device in more detail, we observe the following:

*First*, the appearance of resistive switching in a pristine device is demonstrated by increasing the voltage range of *I-V* sweeps from ±1 V to ±5 V without prior electroforming. The results are summarized in **Figure 2**b, where the resistance in the ON and OFF-states, as well as the $R_{OFF}/R_{ON}$ ratio, are plotted for the various voltage-sweep ranges. From these results we see starting from ± 3V, the resistive switching emerges from the increase of $R_{OFF}$, while $R_{ON}$ remains constant for the increasing sweep range, increasing the resistance ratio up to 40 for ± 5 V.

*Second*, the device can be switched between the two resistance states for more than 1800 cycles, after which the resistance in both the ON and OFF-states degrade leading to a decrease of the $R_{OFF}/R_{ON}$ ratio, see **Figure 2**c.

*Third*, the sweep rate dependence of the switching is shown in **Figure 2**d representing the resistance values of the ON and OFF-state as well as the $R_{OFF}/R_{ON}$ ratio for sweep rates in the range of 10–1000 mV/s. The low-resistance ON-state remains at 2 kΩ for all sweep rates, as the high-resistance OFF-state varies in the range from 43 to 63 kΩ showing almost no sweep rate dependence. These resistive switching characteristics compare to other mixed oxygen anionic-electronic oxides such as well-studied $SrTiO_{3-\delta}$ and $Ba_{0.7}Sr_{0.3}TiO_3$ regarding switching polarity and current magnitude, see Refs. [12] and [49].

*Epitaxial "defect-free" devices*: For the epitaxial $LaFeO_3$ devices we measure a non-linear, double-exponential, current-voltage dependence, **Figure 2**e. We conclude that purely non-linear profiles are observed under the same measurement conditions for the vast majority of epitaxial devices; no resistive switching is observed. Very few electrodes of the crystalline samples exhibited hysteretic *I-V*-response but remain irrelevant in terms of statistics see Supporting Information S3. We interpret

the occurrence of these hysteretic IV-responses to the presence of structural defects within the LaFeO$_3$ bulk of the device, which cannot be excluded in real samples.

Equivalent Circuit Model for the ON and OFF-States for the Amorphous and Epitaxial LaFeO$_3$ Memristive Devices

To gain more insight in the switching mechanism, we employ electrochemical impedance spectroscopy to analyze the frequency dependence of the resistive and capacitive contributions of the memristive switches. Impedance spectra can be modeled with equivalent circuits that consist of a serial connection of a resistor, $R_s$, and a parallel connection of a resistor and a constant phase element, $R_p/CPE$ (**Figure 3**a), mirroring the chemical-physical phenomena that occur in the material and at interfaces. We use the frequency dependence to address the various contributions of the circuit components of the switch:

*i. Electrode contributions to the resistive switching:* The high-frequency axis intercept is attributed to the resistive contributions of the LaNiO$_3$ bottom electrode as well as of the contact resistance from the microprobe tips. It is ~100 Ω independent of the microstructure of the LaFeO$_3$ and resistance state of the amorphous switch, which corresponds to values obtained by DC measurements for the bottom electrode. It further refers to the resistance $R_s$ in the equivalent circuit model.

*ii. LaFeO$_3$ resistive switch analysis for the ON and OFF-memristor states:* For the amorphous device, the low-frequency axis intercept shows a variation of the impedance of over one order of magnitude, **Figure 3**b. Only the resistance $R_p$ changes in the equivalent circuit model, the capacitance of 0.75 µF/cm$^2$ is equal for both memristive states. The capacitance of the epitaxial

memristive switch of 1.46 $\mu F/cm^2$ is about a factor two higher, **Figure 3**c, a value that is in agreement with literature.[50]

Using the equivalent-circuit-model fit of electrochemical impedance spectroscopy results, we can clearly separate the contributions from the electrode and the active resistive switching oxide $LaFeO_3$. It is evident that only the $LaFeO_3$ or its two interfaces participate in the resistive switching, and not the electrodes; the capacitance does not change during the resistance switching. This analysis is further in accordance with the absence of high electric fields in the $LaNiO_3$ layer that are necessary for the switching mechanism to take place, given its high conductivity. Hence, the potential drop occurs only in the $LaFeO_3$ layer and we can draw our conclusions concerning the memristive switching based on structural and chemical changes present in the amorphous state of $LaFeO_3$.[10]

Switching Kinetics of the Amorphous $LaFeO_3$ Memristive Devices: Memory Emulation

To emulate the actual computer memory operation and determine the SET kinetics for the amorphous $LaFeO_3$ memristor device, we discuss the voltage pulsing response. The device resistance is read after a single SET pulse of −5 to −5.8 V amplitude and 100 ns to 1 ms duration, **Figure 4**a. We observe more pronounced resistive switching for higher pulse voltages and longer pulse times, exemplified by the lower read-resistance after the pulse. This is in line with the switching mechanism, where higher electrical fields and the current-induced Joule heating accelerate ionic motion and therefore increase the switching speed and lower the resistance after the SET pulse.[51]

The switching kinetics of the set event were further accessed by extracting the actual switching time from the abrupt changes in the current transients measured during the pulse, **Figure 4**b. The switching time depends exponentially on the applied voltage as shown by the linear relation in the

13

switching time vs. switching voltage diagram, **Figure** 4c, and is in the microseconds range. From this, we learn that a highly nonlinear switching process, with a non-linear acceleration of the ionic movement with bias, occurs in our amorphous $LaFeO_3$ memristive devices, which is a requirement to overcome the voltage-time dilemma for memory operation.[52]

We follow the approach of Menzel et al. and plot the switching kinetics in a semi-logarithmic plot of switching time vs. switching voltage, Figure 4c. A linear fit to the data gives the slope of $\Delta V/\Delta \tau_{log}$ = 524 mV/dec. In memristive devices based on the valence change mechanism generally smaller slopes around 150 mV/dec ($SrTiO_3$)[53], 170 mV/dec ($HfO_x$)[54] and 50 mV/dec ($TiO_x$)[55] have been reported. The lower voltage acceleration in amorphous $LaFeO_3$ compared to the state of the art memristive materials and the switches can point to a different rate limiting step or switching mechanism. Assuming that the limiting step in the SET kinetics is ion hopping, we can link the $\Delta V/\Delta \tau_{log}$ value to the distance over which the voltage drops in the material, a higher $\Delta V/\Delta \tau_{log}$ value implies a longer distance over which the voltage drops.[56] This would suggest that this distance is larger in the amorphous $LaFeO_3$ devices, however further studies are needed in order to fully understand the differences in the switching kinetics.

We conclude the following for the amorphous $LaFeO_3$ memristors based on the cyclic voltammetry, pulse and electrochemical impedance characteristics: *First*, we clearly demonstrate that resistive switching occurs in our pristine amorphous devices without previous electroforming for $LaFeO_3$ and that it is cycling-stable; this is in contrast to the epitaxially grown model device. *Second*, our devices start in the low-resistance ON-state and switch to the OFF-state with a positive voltage. These

results, together with the pulsing characteristic of $\Delta V/\Delta \tau_{log}$ = 524 mV/dec indicate that the switching mechanism is controlled by oxygen ionic carriers and vacancy mediation in the amorphous state of the oxide film. We conclude that the large number of oxygen ionic defects is homogeneously distributed in the amorphous structure of the LaFeO$_3$ film leading to memristors with low variability and good switching performances. *Third*, we exclude crystallization and near-order structural rearrangement in the amorphous phase to be the active driver for the switching mechanism and property of memristance *i.e.* such as in phase-change memories (PCMs)[57] for several reasons: electrochemical impedance analysis provides clear evidence that the capacitance remains unchanged independent of the resistance state of the LaFeO$_3$ memristor device; hence, there is no rearrangement of structural units active in the process. Also, the pristine devices start in the low-resistance ON-state when memristance is probed by cyclic voltammetry, which is opposite to classic PCM mechanisms. The fact that the resistive switching is measurable without an initial electroforming step and an operational memory unit in the pulsing mode makes amorphous LaFeO$_3$ a fascinating novel material component for future memristive memory and computing device integration.

### Probing the Defect States of Defect Modulated LaFeO$_3$ Switching Devices

Memristive behavior is solely observed for the amorphous LaFeO$_3$ structure and inexistent for the epitaxially grown device. Therefore, we focus now on the description of the defect states to understand the charge-transfer mechanism upon resistive switching. First, *the electronic band gap was probed via linear UV-VIS transmission-reflection spectroscopy*, **Figure 5**a, giving information on the electronic structures for the amorphous and epitaxial LaFeO$_3$ oxides in the devices. By extrapolating the linear part to zero for a Tauc plot representation,[58] an electronic band gap of

2.61 eV (±0.7 %) is determined for the epitaxial $LaFeO_3$ film structure and is slightly increased to 2.81 eV (±1.2 %) for the amorphous film. The band gap is close to the expected value for predominant p-type conduction, being 2.1 eV for bulk pellets to 2.6 eV for epitaxial thin-films of $LaFeO_3$.[58, 59] We now probe the activation energy of the amorphous and epitaxial state measuring the electrical conductivity via impedance spectroscopy with respect to temperature, **Figure 5**b. In conformance with the lowered electronic band gap for the epitaxial $LaFeO_3$ device, we report its generally one to two orders of magnitude higher conductivity and lower activation energy of 0.57±0.02 eV, when compared to the amorphous memristive device exhibiting an activation energy of 0.70±0.02 eV. Note that the activation energy of the epitaxial film also agrees with literature.[60]

To investigate the *structural ionic near-order characteristics* of the amorphous and epitaxial devices, we performed Raman spectroscopy, which is known as an efficient, non-destructive technique for structural analyses of oxide thin-films, including heterostructures.[61, 62, 63, 64] **Figure 5**c shows the Raman spectra of the $LaAlO_3$/$LaNiO_3$/$LaFeO_3$ stack for epitaxial and amorphous $LaFeO_3$. Overall, despite the small thickness of the films, the spectra are remarkably well defined, underlining the high quality of the film. $LaAlO_3$ and $LaNiO_3$ both crystallize in the rhombohedral $R\overline{3}c$ structure giving rise to five Raman-active modes: $A_{1g} + 4\,E_g$.[65] The bands at 123, 152 and 486 $cm^{-1}$ are the well-known substrate peaks of $LaAlO_3$,[66] indicated by asterisks in **Figure 5**c. In both spectra, we identify two vibrational bands of $LaNiO_3$ electrodes: the weak tilt mode of $A_g$ symmetry at 217 $cm^{-1}$ and a strong octahedron vibration at 412 $cm^{-1}$ (open diamonds).[67, 68] Both modes are found at slightly higher wavenumbers in comparison with reports on $LaNiO_3$ thin-films on $LaAlO_3$.[65] However, Fowlie et al. reported a hardening of the phonon modes with decreasing film thickness,[69] which fits with our data of a 5 nm-thin $LaNiO_3$ layer for the bottom electrodes of the devices. $LaFeO_3$ is of

orthorhombic *Pnma* structure, *viz.* 24 Raman-active modes: 7 $A_g$ + 5 $B_{1g}$ + 7 $B_{2g}$ + 5 $B_{3g}$.[70] We assign

the Raman bands at 183, 267, 296, and 435 cm$^{-1}$ to $A_g$ modes of LaFeO$_3$ (full diamonds) that are in

good agreement with literature data on LaFeO$_3$ powder samples [71] and the ceramic target reference

spectrum, see Supporting Information S4. The band at 296 cm$^{-1}$ represents a 101$_{pc}$-FeO$_6$ tilt vibration

and does not appear to be shifted compared to the powder samples from literature. The bands at

267 and 296 cm$^{-1}$, characteristic for orthorhombic LaFeO$_3$, are broader and less defined in the

amorphous LaFeO$_3$ device, underlining the higher degree of disorder. However, the simple presence

of these Raman bands in the amorphous device reveals a short-ranger order, which is below the

detection limit of X–ray diffraction. In fact, in contrast to lab X–ray diffraction with a coherence

length of about > 20 lattice parameters, Raman spectroscopy is sensitive to short range order of

about > 5 lattice parameters. On the other hand, a fully amorphous fraction or nano-crystallites

smaller than five lattice constants would lead to a signature very different to the crystal, which is not

observed. Therefore, from X–ray diffraction we might estimate an upper limit of about 15 nm and

from Raman spectroscopy a lower limit of 5 nm of the local order. Furthermore, a broad band is

present at about 650 cm$^{-1}$ in the amorphous device. There is a debate in the literature about the

origin of this band, whether it is defect activated,[72] originating from oxygen vacancies,[73] IR LO

phonon bands,[74] Jahn-Teller distortions,[75] or a disordered anion lattice.[76] We interpret the higher

band intensity as an indication that the octahedra persist in the amorphous state. These vibrations

remain visible in highly defectuous systems since they are molecular-like vibrations.

To verify the possible involvement of *changes of the transition metal iron oxidation states* for

amorphous LaFeO$_3$ to contribute to the memristive characteristics, in contrast to the non-switching

devices with epitaxial LaFeO$_3$, XPS measurements were performed. The according spectra of the

amorphous and epitaxial LaFeO$_3$ samples are provided in Supporting Information S5 and compared with a target reference measurement. The quantitative analysis reveals near-stoichiometric composition for both microstructures, with slight iron excess in both cases and no oxygen deficiency could be measured in neither of the samples. Iron is predominantly present in the Fe(III) state independently on the crystallinity state of the LaFeO$_3$ film. From these measurements we can exclude big variations in the transition metal iron valence state and electronic band structure to contribute to the superior switching of the amorphous memristors when compared to the epitaxially grown LaFeO$_3$ devices.

From literature we know that *oxygen diffusivity* can be significantly enhanced in lattice defectuous zones such as grain boundaries[77] for perovskites. Also, for binary oxides, the oxygen diffusion extrapolated to room temperature is about 15 orders of magnitude larger in the amorphous material when compared to crystalline counterparts such as Al$_2$O$_3$ [78] or SiO$_2$,[79] when probed for Arrhenius activation. Oxygen tracer diffusion experiments were performed at 450°C for 60 min using 200 mbar $^{18}$O$_2$ to probe the surface exchange and diffusivity of oxygen in both the amorphous and epitaxial microstructures. The normalized concentration of the $^{18}$O tracer, which was calculated from ToF-SIMS depth profiles, is shown against the sputter depth in **Figure 5**d. There, the dotted blue line represents the bottom interface of the LaFeO$_3$ film. The tracer concentration profile reveals a strongly enhanced oxygen diffusion coefficient in the highly defectuous amorphous film compared to its epitaxial counterpart throughout the whole thickness of the LaFeO$_3$ layer. By fitting the concentration profiles, a diffusion coefficient of D* = 1.3×10$^{-14}$ cm$^2$/s and a surface exchange coefficient of and k* = 1.8×10$^{-11}$ cm/s can be determined for the amorphous LaFeO$_3$ film, which are an order of magnitude higher than in the epitaxial film. Consequently, either the mobility, the

concentration of oxygen vacancies or both are strongly enhanced in the amorphous compared to the epitaxial film. On the other hand, investigation of the *electronic band gap* and *charge transport, Raman near-order vibrations* and *Fe oxidation state* for the amorphous $LaFeO_3$ memristor device provide combined evidence that the electronic states are not strongly affected by the change in microstructure. Evidence combined through this work highlights the potential of amorphous $LaFeO_3$ to be an excellent novel memristor material with no requirement for electroforming and high stability to induce oxygen-vacancy migration as operating carriers. We unequivocally show that the amorphous structure favors the transport of the oxygen ionic carriers for memristive oxides, a prerequisite for faster and better performing next-generation non-volatile memories.

**Conclusion**

In the sum of this work, the ability of amorphous oxides to reveal more than one order of magnitude higher oxygen ionic diffusion for memristive computation than its crystalline counter-part has been clearly demonstrated on the model $LaFeO_3$ systems and discussed towards electronic state changes and exchange kinetics. Memory emulation and voltage-pulsing combined with oxygen vacancy diffusion ($^{18}O$-study) evidence that the amorphous near-order is advantageous to promote resistance modulation for memristive devices, for which we report a stable resistance ratio $R_{OFF}/R_{ON}$ up to 100. We can exclude changes in electronic structures as well as ion states of Fe to account for the memristive function of the devices when modulating the ionic near-order of $LaFeO_3$ from epitaxial to amorphous, a conclusion based on X–ray, optical and Raman spectroscopical evidence. From a broader perspective, the finding of increased ionic diffusion for the amorphous perovskite films and improved memristive performance has far-reaching consequences both for applications and fundamental material science. Despite the wide integration of amorphous oxides to memristive circuits, we present here the first material example of a system with modulated ionic bonding structures ranging from amorphous to epitaxial $LaFeO_3$ and study the memristance changes involved. Excitingly, we show that oxides in the amorphous state have accelerated ionic migration at high local electric fields at room temperature when compared to crystalline microstructure. Till date it is widely accepted for high-temperature oxide films that amorphous grain boundaries can have orders of magnitude altered ionic migration due to high defect density when compared to grains at elevated temperatures. Yet, memristive characteristics at room temperature and at high electric fields such as presented on the example of amorphous vs. epitaxial $LaFeO_3$ are still unique. Given the rich nature of disordered states for amorphous oxide films, this opens future avenues for the quest

of optimal amorphous oxide structures as promising material engineering opportunities for future non-volatile memories and neuromorphic memristive computer hardware.

**Experimental Section**

Electrochemical cells for the resistive switching devices were fabricated by subsequent pulsed laser depositions of a $LaNiO_3$ electrode and $LaFeO_3$ switching oxide on a $LaAlO_3$ (100) single crystal, and an electron-beam evaporated platinum as the top electrode. The implication of the ionic and electronic defect structures of $LaFeO_3$ on resistive switch performances was in focus.

*Material and Resistive Switching Device Synthesis*

For the resistive switches, bilayers of $LaNiO_3$ (LNO)/$LaFeO_3$ (LFO) were grown as a set of bottom electrode/switching oxides on $LaAlO_3$ (LAO) (100) single-crystal substrates (CrysTec GmbH, Germany) by pulsed laser deposition (PLD, home built) with a KrF 248 nm excimer laser (COMPex Pro 220 F) operated at a target-substrate distance of 70 mm. The 20-nm-thick LFO switching oxide was deposited with different microstructures. Amorphous films were deposited at a laser fluence of 1.1 $J/cm^2$ with 5 Hz repetition rate at an oxygen pressure of $6 \cdot 10^{-2}$ mbar at 500°C for 1h15 isothermal hold (22,500 shots). 20-nm-thick epitaxial single-crystal LFO was achieved by increasing the deposition temperature to 700°C at a laser fluence of 1.35 $J/cm^2$ with 2 Hz repetition rate at an oxygen pressure of $1 \cdot 10^{-3}$ mbar for 62.5 min isothermal hold (7,500 shots).

The LNO electrode was grown at a laser fluence of 0.9 $J/cm^2$ and a repetition rate of 2 Hz at $3 \cdot 10^{-2}$ mbar oxygen pressure for a 15-minute hold at 500°C (1,800 shots). The bilayer electrode/switching oxide films were cooled down to room temperature under 300 mbar oxygen with 10°C/min.

The PLD targets of LNO and LFO were prepared from a citrate-nitrate Pechini route, powder compaction, and sintering. Pechini synthesis was based on stoichiometric mixing of the chemicals being $La(NO_3)_3 \cdot 6H_2O$ (99.9%, Alfa Aesar), $Ni(NO_3)_2 \cdot 6H_2O$ (99.9%, Strem chemicals), Fe (>99.99%, Sigma-Aldrich), citric acid (99%, Aldrich), ethylene glycol (99.5%, Fluka) and nitric acid (puriss p.a. Sigma-Aldrich). Calcination was carried out at 800°C and 600°C for the LFO and LNO powders, respectively. The LFO powder was first uniaxially and subsequently isostatically pressed at 350 MPa for 2 min and sintered at 1300°C for 24 h with a rate of ±2°C/min. The LNO powder was compacted at 15 kN using a hot press at 700°C. The target was subsequently annealed at 800°C in air to remove carbon traces from the hot press tools.

Metal top electrode patterns were fabricated by e-beam evaporation on the PLD bottom electrode-switching oxide bilayer structures. First, the samples were cleaned in an $O_2$ plasma-asher (Technics Plasma TePla 100 asher-system) at 100 W and 1 mbar oxygen pressure for 60 s. The top platinum electrodes of 80 nm thickness were then deposited through a stainless steel shadow mask by means of electron beam evaporation (Plassys MEB 550, France).

*Material Structural Characterization*

The oxide PLD target phase purity was confirmed by XRD (Bruker D8) at a Cu Kα wavelength, see Supporting Information S4. High-resolution XRD (Seifert XRD 3003 PTS-HR) at Cu Kα wavelength equipped with three Ge (220) monochromators was used to characterize the phases and degree of epitaxy for the PLD-grown thin-films relative to the single crystal orientation. For this, the LNO and LFO PLD films were oriented to the (002) LAO substrate peak as a reference. AFM (Cypher S, Asylum Research) scans of the surface morphologies were taken using AC tapping mode with an Arrow NCR-tip (NanoWorld). Transmission electron microscopy (TEM) and Scanning Transmission Electron

22

Microscopy (STEM) measurements were performed on Focused Ion Beam (FIB)-cut lamellas with an FEI Talos F200X at 200 kV. The TEM lamellas were cut and thinned using a 30 kV, 300 pA gallium beam (NVision 40, Zeiss).

*Ionic Near-Order and Electronic Band Structure Characterization*

The anionic-cationic near-order structure was probed using a confocal WITec alpha300 R Raman microscope instrument (WITec, Germany) equipped with a 457 nm wavelength laser for excitation and a spectral resolution of 0.4 cm$^{-1}$. The optical band gap of the LFO films was probed by optical transmission and reflection spectroscopy using a Jasco MSV-370 UV/VIS/NIR micro-spectrophotometer at room temperature in the range of 200-2500 nm with a spectral resolution of 1 nm. The direct band gap value was determined by plotting $(\alpha h\nu)^2$ as a function of the photon energy $h\nu$ (Tauc plot) and extrapolating the linear portion of the curve to $(\alpha h\nu)^2 = 0$.

*Electrochemical Characterization of Resistive Switch Device Elements*

In this study, we selected three types of electrical and electrochemical characterization, being *cyclic voltammetry* to characterize the resistive switching performance of the model devices, *electrochemical impedance spectroscopy* to study the high and low-resistance states of the resistive switch in more detail and *pulsing experiments* to investigate the device performance and SET kinetics.

The electric measurements were carried out in an own assembled microprobe-setup employing in parallel a light microscope and electrochemical analysis with either a Keithley SMU 2601B, an electrochemical impedance spectrometer (Gamry Instruments, Reference 600$^{TM}$) or the Keithley 4200 semiconductor characterization system in air. High-level impedance measurements were

carried out in an own constructed shielded box in a noise-damped room. In all measurements, the bias voltage was applied to the platinum top electrode on LFO, and the LNO bottom electrode was grounded via microprobe tips. Top platinum microelectrodes were contacted by self-made platinum tips and the LNO bottom electrode by platinum tips and silver paste.

Cyclic voltammetry on model resistive switching device testing

Cyclic voltammetry measurements were carried out between ±5 V (±250 MVm$^{-1}$) with 500 mVs$^{-1}$ unless otherwise indicated. The resistance of the resulting *I-V* curves is determined by linearly fitting the *I-V*-curve at the origin for both increasing and decreasing voltages. In total 12 samples have been tested, while each sample consists of an array of microelectrodes allowing for about 4×25 independent resistive switching devices (4 different electrode sizes) on the same sample.

Impedance spectroscopy to characterize the resistance ON and OFF-states of the resistive switching devices

The resistance states were set by applying a voltage pulse of ±4 V for a duration of 1 s. Electrochemical impedance spectra were recorded with 10 mV AC amplitude in air without DC bias for a frequency range of 1 MHz to 10 Hz. The electrochemical impedance data were analyzed with an equivalent circuit model using a set of ***R**esistance-(**R**esistance/**C**onstant **P**hase **E**lement), R$_s$-(R$_p$/CPE)* elements using ZView software. For these, the capacitance of the constant phase element was calculated from the fit parameters via $C = \left(R_p^{1-n}Q\right)^{1/n}$,[80] whereby $R_p$ is the resistance, *n* the exponent equaling 1 for a capacitor and 0 for a resistance, and Q$_2$ the constant phase element.

Activation energy

The activation energy of the devices was measured between room temperature and 270°C in air in a home-built microprobe station. The devices were glued on a sapphire substrate using silver paste to ensure good thermal contact. The temperature was measured using a thermocouple placed on a dummy $LaAlO_3$ substrate glued in the same manner. The sample was thermally equilibrated for at least 5 minutes. The results of the first cooling cycle are taken into consideration. Electrochemical impedance spectra were recorded as mentioned above. Only $R_p$, corresponding to the $LaFeO_3$ resistance, was taken into account.

Pulsing measurements to investigate the SET kinetics

The performance of the amorphous devices was probed with short voltage pulses combined with longer DC RESET profiles using the Keithley 4200 semiconductor characterization system. A Remote Preamplifier/Switch-Module attached to custom probes was used to switch between the quasi-static and pulsing modes. The device was reset to the OFF-state by applying a voltage of +4 V for 10 s. The SET-pulse duration is varied between 1 ms and 2 µs and the SET-voltage between −5 V and −5.8 V. The device resistance after the SET pulses was determined from a 0.1 s reading pulse of 0.5 V. The measured current of the reading pulse was averaged between 50 and 90% of the pulse width to get a single valued resistance.

*X–ray Photoelectron Spectroscopy*

X–ray photoelectron spectroscopy (XPS) was exploited for the chemical state identification and for the semi-quantitative composition analysis of the thin-film devices as well as of the ceramic target reference. A PHI Quantera$^{SXM}$ spectrometer (ULVAC-PHI, Chanhassen, MN, USA) equipped with an AlKα monochromatic source, whose beam size ranges from 5 to 200 µm, was used. In the present

work, a beam diameter of 109 µm was used at 25 W. The emission angle was at 45°. The spectrometer has a low-voltage argon ion gun and a sample neutralizer for charge compensation. The linearity of the binding energy scale was checked using sputter-cleaned gold, silver, and copper as reference materials according to ISO15472: 2010 reapproved in 2015. The accuracy was found to be ±0.1 eV. The residual pressure was always below $5 \times 10^{-7}$ Pa during the experiments.

Survey spectra were acquired in a fixed analyzer transmission (FAT) mode using a pass energy (PE) of 280 eV, while the high-resolution spectra were collected setting the PE to 69 eV; the full width at half-maximum of the peak height, FWHM, of the silver $Ag3d_{5/2}$ signal was 0.81 eV. X–ray excited secondary electron images (SXI) were used in order to visualize the topography and, thus, to be able to collect small-area XPS spectra from the features present in the sample. The electron neutralizer was used in order to compensate for sample charging, and the spectra were further corrected with reference to adventitious aliphatic carbon at 285.0 eV.

Data processing

The spectra were processed using CasaXPS software (version 2.3.16, Casa Software Ltd, Wilmslow, Cheshire, UK). The background subtraction was performed using the Shirley-Sherwood iterative method. The product of Gaussian and Lorentzian functions was used for the curve-fittings.

The XP-spectra were fitted following the Gupta and Sen [81, 82] and Grosvenor et al. approach.[83] The relative positions, heights, and FWHM of the sub-peaks were kept constant, only the peak height of the first component was varied to optimize the fit. This approach is analogous to that followed by Fantauzzi et al.[84] and the results of the fits of pure oxides analyzed in the same conditions are consistent with the model. This assumption is also substantiated by the fact that perovskites and

hematite are isostructural oxides. The FWHM in α-compounds was observed to be smaller than in the γ-compounds and this was attributed to differences in the orientation of the Fe(III) cations in the two sets of compounds.[83] This only depends on the charge of the iron ion, and it is independent of the ligand electronegativity. Gupta and Sen based their calculations on the assumption of a free ion, therefore the same intensity was used for Fe (III) and Fe(III)OOH. The curve fitting parameters are reported in Table 1. The FWHM of peak 1 was set to 1.6 according to the reference oxides acquired using the same experimental conditions (*i.e.* pass energy of 69 eV). The curve fitting was carried out assuming the presence of Fe (II) and Fe (III) oxides.

**Table 1. Fe 2p$_{3/2}$ peak fitting parameters used to fit the Fe(II) and Fe(III) compounds based on Gupta and Sen (GS) multiplet peak parameters from Grosvenor et al.[83] The notation {1} indicates the constraint to the parameters of peak 1. The model function was a Gaussian/Lorentzian product function, and the G/L ratio was set equal to 45 for all components.**

| | | α-Fe$_2$O$_3$ | FeO | FeOOH |
|---|---|---|---|---|
| Peak 1 | Pos. (eV) | 709.8 | 708.4 | 710.2 |
| | FWHM | 1.6 | 1.6 | 1.6 |
| | Intensity | Free | Free | Free |
| Peak 2 | Pos. (eV) | {1}+0.9 | {1}+1.3 | {1}+1.0 |
| | FWHM | {1}×1.2 | {1}×1.14 | {1}×0.92 |
| | Intensity | {1}×0.76 | {1}×1.29 | {1}×0.76 |

| | | | | |
|---|---|---|---|---|
| Peak 3 | Pos. (eV) | {1}+1.6 | {1}+2.5 | {1}+1.9 |
| | FWHM | {1}×1.2 | {1}×1.14 | {1}×1.08 |
| | Intensity | {1}×0.49 | {1}×0.48 | {1}×0.49 |
| Peak 4 | Pos. (eV) | {1}+2.5 | | {1}+3.0 |
| | FWHM | {1}×1.4 | | {1}×1.08 |
| | Intensity | {1}×0.25 | | {1}×0.25 |

The shake-up satellite of the Fe (II) was located at 7 eV higher binding energy values in respect of the main signal; its FWHM was constrained at 3.3 eV, and the intensity was found to be 8% of the first signal. The shake-up satellite of the Fe (III) was constrained at 718.55 eV, the FWHM was equal to 1.9 eV, and no constraints were applied for the peak intensity since this signal is well-defined.

The semi-quantitative analyses were carried out using the signals of the valence spectral region; peak areas were only corrected for the photoionization cross-sections following Band et al.[85]

*$^{18}O_2$ Tracer Diffusion*

Isotope exchange experiments were performed at 450°C in 200 mbar dry $^{18}O_2$ (97.1 % isotope enriched, CAMPRO) in a special quartz setup. Subsequent depth profiling of the oxygen isotope distribution was performed on a TOF.SIMS 5 instrument (ION-TOF) using 25 kV $Bi_3^{++}$ primary ions (ca. 0.03 pA), 2 kV $Cs^+$ for sputtering (ca. 120 nA) and a low energy electron gun (20 V) for charge

compensation. Negative secondary ions were measured and the signals of $16O^-$ and $18O^-$ were used to calculate isotope ratios. Details on the used measurement mode ("CBA" mode) are given in Refs.[86] and [87] Areas of 100 μm × 100 μm were analyzed and sputter crates were 300 μm × 300 μm wide. Depth profiles were fitted, assuming a blocking substrate, by an iterative method described in Refs.[88] and [89].

# WILEY-VCH

**Supporting Information**

Supporting Information is available from the Wiley Online Library or from the author.

**Author Contributions**

R.S., M.K., and J.L.M.R. conceived and designed the experiments. R.S. carried out the experiments and J.L.M.R. directed the research. M.K. performed and interpreted the tracer diffusion experiments and E.S. performed and interpreted the pulsing experiments. M.T. and M.F. contributed with their expertise on lasers and PLD film growth. A.R. performed the XPS measurements processed them and interpreted the results. M.W. and J.K. strongly

supported the Raman analysis. The manuscript was written through contributions of all authors. All authors have given approval to the final version of the manuscript.

**Funding Sources**

Received: ((will be filled in by the editorial staff))
Revised: ((will be filled in by the editorial staff))
Published online: ((will be filled in by the editorial staff))

References

[1]     M. B. Taylor, *Micro, IEEE* **2013**, 33, 8.

[2]     R. Stevenson, *Spectrum, IEEE* **2013**, 50, 34.

[3]     F. L. Traversa, M. Di Ventra, *IEEE Trans. Neural Netw. Learn. Syst.* **2015**, DOI: 10.1109/TNNLS.2015.2391182.

[4]     G. I. Meijer, *Science* **2008**, 319, 1625.

[5]     Z. Wang, S. Joshi, S. E. Savel'ev, H. Jiang, R. Midya, P. Lin, M. Hu, N. Ge, J. P. Strachan, Z. Li, Q. Wu, M. Barnell, G.-L. Li, H. L. Xin, R. S. Williams, Q. Xia, J. J. Yang, *Nat. Mater.* **2016**, advance online publication.

[6]     L. Chua, *Semicond. Sci. Technol.* **2014**, 29, 104001.

[7]     R. Waser, M. Aono, *Nat. Mater.* **2007**, 6, 833.

[8]     D. Cooper, C. Baeumer, N. Bernier, A. Marchewka, C. La Torre, R. E. Dunin-Borkowski, S. Menzel, R. Waser, R. Dittmann, *Adv. Mater.* **2017**, 1700212.

[9]     R. Schmitt, J. Spring, R. Korobko, J. L. M. Rupp, *ACS Nano* **2017**, 11, 8881.

[10]    J. J. Yang, D. B. Strukov, D. R. Stewart, *Nat. Nanotechnol.* **2013**, 8, 13.

[11]    Y. Watanabe, J. G. Bednorz, A. Bietsch, C. Gerber, D. Widmer, A. Beck, S. J. Wind, *Appl. Phys. Lett.* **2001**, 78, 3738.

[12]    K. Szot, W. Speier, G. Bihlmayer, R. Waser, *Nat. Mater.* **2006**, 5, 312.

[13]    C. Baeumer, C. Schmitz, A. H. H. Ramadan, H. Du, K. Skaja, V. Feyer, P. Muller, B. Arndt, C.-L. Jia, J. Mayer, R. A. De Souza, C. Michael Schneider, R. Waser, R. Dittmann, *Nat. Commun.* **2015**, 6.

[14]    M. Kubicek, R. Schmitt, F. Messerschmitt, J. L. M. Rupp, *ACS Nano* **2015**, 9, 10737.

[15]    C. Baeumer, R. Valenta, C. Schmitz, A. Locatelli, T. O. Menteş, S. P. Rogers, A. Sala, N. Raab, S. Nemsak, M. Shim, C. M. Schneider, S. Menzel, R. Waser, R. Dittmann, *ACS Nano* **2017**, 11, 6921.

[16]    F. Messerschmitt, M. Kubicek, J. L. M. Rupp, *Adv. Funct. Mater.* **2015**, 25, 5117.

[17]    X. Sun, G. Li, L. Chen, Z. Shi, W. Zhang, *Nanoscale Research Letters* **2011**, 6, 1.

[18]    H. Nili, S. Walia, S. Balendhran, D. B. Strukov, M. Bhaskaran, S. Sriram, *Adv. Funct. Mater.* **2014**, 24, 6741.

[19]    H. Nili, S. Walia, A. E. Kandjani, R. Ramanathan, P. Gutruf, T. Ahmed, S. Balendhran, V. Bansal, D. B. Strukov, O. Kavehei, M. Bhaskaran, S. Sriram, *Adv. Funct. Mater.* **2015**, 25, 3172.

[20]    N. Hussein, A. Taimur, W. Sumeet, R. Rajesh, K. Ahmad Esmaielzadeh, R. Sergey, K. Jeeson, K. Omid, B. Vipul, B. Madhu, S. Sharath, *Nanotechnology* **2016**, 27, 505210.

[21]    J. Fleig, *Solid State Ionics* **2003**, 161, 279.

[22]    J. L. M. Rupp, L. J. Gauckler, *Solid State Ionics* **2006**, 177, 2513.

[23]    F. Aguesse, A.-K. Axelsson, P. Reinhard, V. Tileli, J. L. M. Rupp, N. M. Alford, *Thin Solid Films* **2013**, 539, 384.

[24]    J. L. M. Rupp, B. Scherrer, N. Schäuble, L. J. Gauckler, *Adv. Funct. Mater.* **2010**, 20, 2807.

[25]    V. Metlenko, A. H. H. Ramadan, F. Gunkel, H. Du, H. Schraknepper, S. Hoffmann-Eifert, R. Dittmann, R. Waser, R. A. De Souza, *Nanoscale* **2014**, 6, 12864.

[26]    D. Marrocchelli, L. Sun, B. Yildiz, *J. Am. Chem. Soc.* **2015**, 137, 4735.

[27]    I. Garbayo, M. Struzik, W. J. Bowman, R. Pfenninger, E. Stilp, J. L. M. Rupp, *Adv. Energy Mater.*, DOI: 10.1002/aenm.2017022651702265.

[28]    D. Ehre, H. Cohen, V. Lyahovitskaya, I. Lubomirsky, *Phys. Rev. B* **2008**, 77, 184106.

[29]    F. Messerschmitt, M. Kubicek, S. Schweiger, J. L. M. Rupp, *Adv. Funct. Mater.* **2014**, 24, 7448.

[30]    M. Schie, M. P. Müller, M. Salinga, R. Waser, R. A. D. Souza, *The Journal of Chemical Physics* **2017**, 146, 094508.

[31]    K. Shibuya, R. Dittmann, S. Mi, R. Waser, *Adv. Mater.* **2010**, 22, 411.

[32]    D. S. Shang, L. D. Chen, Q. Wang, W. D. Yu, X. M. Li, J. R. Sun, B. G. Shen, *J. Appl. Phys.* **2009**, 105.

[33]    J.-W. Yoon, J. H. Yoon, J.-H. Lee, C. S. Hwang, *Nanoscale* **2014**, 6, 6668.

[34]    J. Suntivich, H. A. Gasteiger, N. Yabuuchi, H. Nakanishi, J. B. Goodenough, Y. Shao-Horn, *Nat. Chem.* **2011**, 3, 546.

[35]    A. H. Bork, M. Kubicek, M. Struzik, J. L. M. Rupp, *Journal of Materials Chemistry A* **2015**, 3, 15546.

[36]    S. Bagdzevicius, K. Maas, M. Boudard, M. Burriel, *J. Electroceram.* **2017**, DOI: 10.1007/s10832-017-0087-91.

[37]    I. Wærnhus, P. E. Vullum, R. Holmestad, T. Grande, K. Wiik, *Solid State Ionics* **2005**, 176, 2783.

[38]    I. Wærnhus, T. Grande, K. Wiik, *Solid State Ionics* **2005**, 176, 2609.

[39]    M. D. Scafetta, A. M. Cordi, J. M. Rondinelli, S. J. May, *J. Phys.: Condens. Matter* **2014**, 26, 505502.

[40]    M. Kubicek, A. H. Bork, J. L. M. Rupp, *Materials Chemistry A* **2017**, in press.

[41]    A. Demont, S. Abanades, E. Beche, *The Journal of Physical Chemistry C* **2014**, 118, 12682.

[42]    K. Huang, H. Y. Lee, J. B. Goodenough, *J. Electrochem. Soc.* **1998**, 145, 3220.

[43]    P. Ciambelli, S. Cimino, L. Lisi, M. Faticanti, G. Minelli, I. Pettiti, P. Porta, *Applied Catalysis B: Environmental* **2001**, 33, 193.

[44]    N. N. Toan, S. Saukko, V. Lantto, *Physica B: Condensed Matter* **2003**, 327, 279.

[45]    A. Tsurumaki-Fukuchi, H. Yamada, A. Sawa, *Appl. Phys. Lett.* **2013**, 103.

[46]    A. Tsurumaki-Fukuchi, H. Yamada, A. Sawa, *Appl. Phys. Lett.* **2014**, 104.

[47]    P. Zhang, C. Gao, F. Lv, Y. Wei, C. Dong, C. Jia, Q. Liu, D. Xue, *Appl. Phys. Lett.* **2014**, 105, 152904.

[48]    C. Gao, P. Zhang, C. Zhang, C. Dong, C. Jiang, Q. Liu, D. Xue, *Ceram. Int.* **2015**, DOI: http://dx.doi.org/10.1016/j.ceramint.2015.03.201.

[49]    R. Oligschlaeger, R. Waser, R. Meyer, S. Karthäuser, R. Dittmann, *Appl. Phys. Lett.* **2006**, 88.

[50]    G. Sethi, B. Bontempo, E. Furman, M. W. Horn, M. T. Lanagan, S. S. N. Bharadwaja, J. Li, *J. Mater. Res.* **2011**, 26, 745.

[51]    D. Ielmini, F. Nardi, S. Balatti, *IEEE Trans. Electron Devices* **2012**, 59, 2049.

[52]    R. Waser, R. Dittmann, G. Staikov, K. Szot, *Adv. Mater.* **2009**, 21, 2632.

[53]    K. Fleck, U. Böttger, R. Waser, S. Menzel, *Electron Device Letters, IEEE* **2014**, 35, 924.

[54]    M. G. Cao, Y. S. Chen, J. R. Sun, D. S. Shang, L. F. Liu, J. F. Kang, B. G. Shen, *Appl. Phys. Lett.* **2012**, 101, 203502.

[55]    F. Alibart, L. Gao, B. D. Hoskins, D. B. Strukov, *Nanotechnology* **2012**, 23, 075201.

[56]    S. Menzel, U. Böttger, M. Wimmer, M. Salinga, *Adv. Funct. Mater.* **2015**, 25, 6306.

[57]    M. Wuttig, N. Yamada, *Nat. Mater.* **2007**, 6, 824.

[58]    M. D. Scafetta, Y. J. Xie, M. Torres, J. E. Spanier, S. J. May, *Appl. Phys. Lett.* **2013**, 102, 081904.

[59]    R. Köferstein, L. Jäger, S. G. Ebbinghaus, *Solid State Ionics* **2013**, 249–250, 1.

[60]    H. Yamamura, H. Haneda, S.-I. Shirasaki, K. Takada, *J. Solid State Chem.* **1981**, 36, 1.

[61]    D. A. Tenne, A. Bruchhausen, N. D. Lanzillotti-Kimura, A. Fainstein, R. S. Katiyar, A. Cantarero, A. Soukiassian, V. Vaithyanathan, J. H. Haeni, W. Tian, D. G. Schlom, K. J. Choi, D. M. Kim, C.

B. Eom, H. P. Sun, X. Q. Pan, Y. L. Li, L. Q. Chen, Q. X. Jia, S. M. Nakhmanson, K. M. Rabe, X. X. Xi, *Science* **2006**, 313, 1614.

[62]     J. Kreisel, M. C. Weber, N. Dix, F. Sánchez, P. A. Thomas, J. Fontcuberta, *Adv. Funct. Mater.* **2012**, 22, 5044.

[63]     S. Schweiger, M. Kubicek, F. Messerschmitt, C. Murer, J. L. M. Rupp, *ACS Nano* **2014**, 8, 5032.

[64]     S. Schweiger, R. Pfenninger, W. J. Bowman, U. Aschauer, J. L. M. Rupp, *Adv. Mater.* **2017**, DOI: 10.1002/adma.2016050491605049.

[65]     M. C. Weber, M. Guennou, N. Dix, D. Pesquera, F. Sánchez, G. Herranz, J. Fontcuberta, L. López-Conesa, S. Estradé, F. Peiró, J. Iñiguez, J. Kreisel, *Phys. Rev. B* **2016**, 94, 014118.

[66]     M. V. Abrashev, A. P. Litvinchuk, M. N. Iliev, R. L. Meng, V. N. Popov, V. G. Ivanov, R. A. Chakalov, C. Thomsen, *Phys. Rev. B* **1999**, 59, 4146.

[67]     N. Chaban, M. Weber, S. Pignard, J. Kreisel, *Appl. Phys. Lett.* **2010**, 97, 031915.

[68]     G. Gou, I. Grinberg, A. M. Rappe, J. M. Rondinelli, *Phys. Rev. B* **2011**, 84, 144101.

[69]     J. Fowlie, M. Gibert, G. Tieri, A. Gloter, J. Íñiguez, A. Filippetti, S. Catalano, S. Gariglio, A. Schober, M. Guennou, J. Kreisel, O. Stéphan, J.-M. Triscone, *Adv. Mater.* **2017**, DOI: 10.1002/adma.2016051971605197.

[70]     E. Kroumova, M. I. Aroyo, J. M. Perez-Mato, A. Kirov, C. Capillas, S. Ivantchev, H. Wondratschek, *Phase Transitions* **2003**, 76, 155.

[71]     M. C. Weber, M. Guennou, H. J. Zhao, J. Íñiguez, R. Vilarinho, A. Almeida, J. A. Moreira, J. Kreisel, *Phys. Rev. B* **2016**, 94, 214103.

[72]     M. N. Iliev, M. V. Abrashev, H. G. Lee, V. N. Popov, Y. Y. Sun, C. Thomsen, R. L. Meng, C. W. Chu, *Phys. Rev. B* **1998**, 57, 2872.

[73]     I. Kosacki, J. Schoonman, M. Balkanski, *Solid State Ionics* **1992**, 57, 345.

[74]     J. Andreasson, J. Holmlund, R. Rauer, M. Käll, L. Börjesson, C. S. Knee, A. K. Eriksson, S.-G. Eriksson, M. Rübhausen, R. P. Chaudhury, *Phys. Rev. B* **2008**, 78, 235103.

[75]     A. I. Mohammad, X. Yujun, D. S. Mark, J. M. Steven, E. S. Jonathan, *J. Phys.: Condens. Matter* **2015**, 27, 155401.

[76]     W.-Y. Lee, H. J. Yun, J.-W. Yoon, *J. Alloys Compd.* **2014**, 583, 320.

[77]     A. M. Saranya, D. Pla, A. Morata, A. Cavallaro, J. Canales-Vázquez, J. A. Kilner, M. Burriel, A. Tarancón, *Adv. Energy Mater.* **2015**, 5, 1500377.

[78]     N. Toshihide, Y. Tetsuji, N. Masayasu, I. Minoru, H. Tsuyoshi, T. Akira, *Jpn. J. Appl. Phys.* **2003**, 42, 7205.

[79]     J. Rodríguez-Viejo, F. Sibieude, M. T. Clavaguera-Mora, C. Monty, *Appl. Phys. Lett.* **1993**, 63, 1906.

[80]     J. Fleig, *Solid State Ionics* **2002**, 150, 181.

[81]     R. P. Gupta, S. K. Sen, *Phys. Rev. B* **1974**, 10, 71.

[82]     R. P. Gupta, S. K. Sen, *Phys. Rev. B* **1975**, 12, 15.

[83]     A. P. Grosvenor, B. A. Kobe, M. C. Biesinger, N. S. McIntyre, *Surf. Interface Anal.* **2004**, 36, 1564.

[84]     M. Fantauzzi, A. Pacella, D. Atzei, A. Gianfagna, G. B. Andreozzi, A. Rossi, *Analytical and Bioanalytical Chemistry* **2010**, 396, 2889.

[85]     I. M. Band, Y. I. Kharitonov, M. B. Trzhaskovskaya, *At. Data Nucl. Data Tables* **1979**, 23, 443.

[86]     G. Holzlechner, M. Kubicek, H. Hutter, J. Fleig, *J. Anal. At. Spectrom.* **2013**, 28, 1080.

[87]     M. Kubicek, G. Holzlechner, A. K. Opitz, S. Larisegger, H. Hutter, J. Fleig, *Appl. Surf. Sci.* **2014**, 289, 407.

[88]     M. W. den Otter, L. M. van der Haar, H. J. M. Bouwmeester, *Solid State Ionics* **2000**, 134, 259.

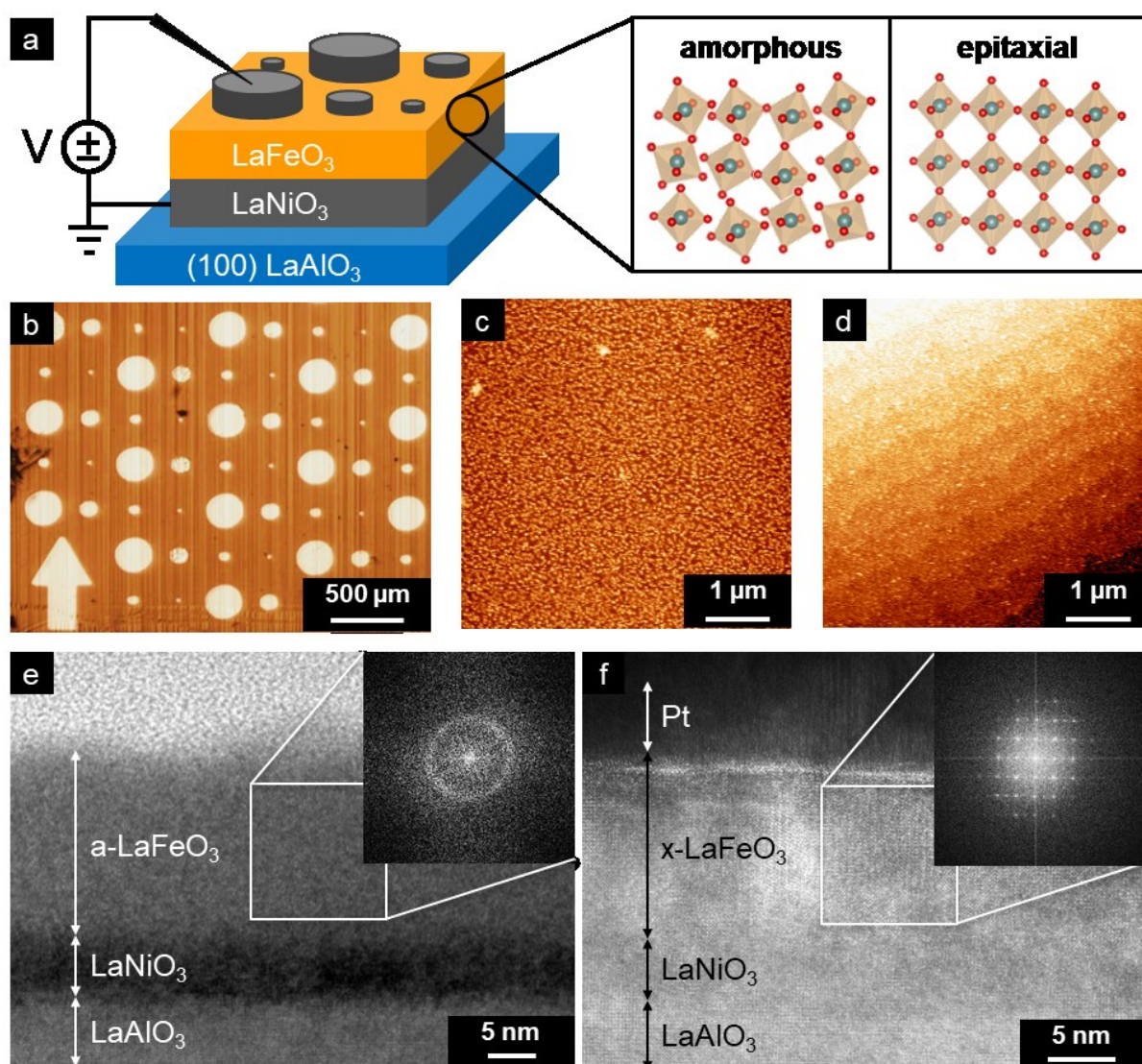[89]     M. Kubicek, Z. Cai, W. Ma, B. Yildiz, H. Hutter, J. Fleig, *ACS Nano* **2013**, 7, 3276.

**Figure 1. Structural defects analysis of the LaFeO$_3$ resistive switching devices. a) Schematic of the model structure device. b) Optical micrograph showing the differently sized Pt top electrodes. c-d) AFM scan of the amorphous and crystalline LaFeO$_3$ device respectively (5x5 μm$^2$ scan area). The terraces in (d) resolve the substrate miscut. The amplitude of the displayed color scale is 5 and 3 nm respectively. e-f) TEM scan showing the amorphous and epitaxial growth of LaFeO$_3$ respectively. The diffraction pattern is shown as an inset.**
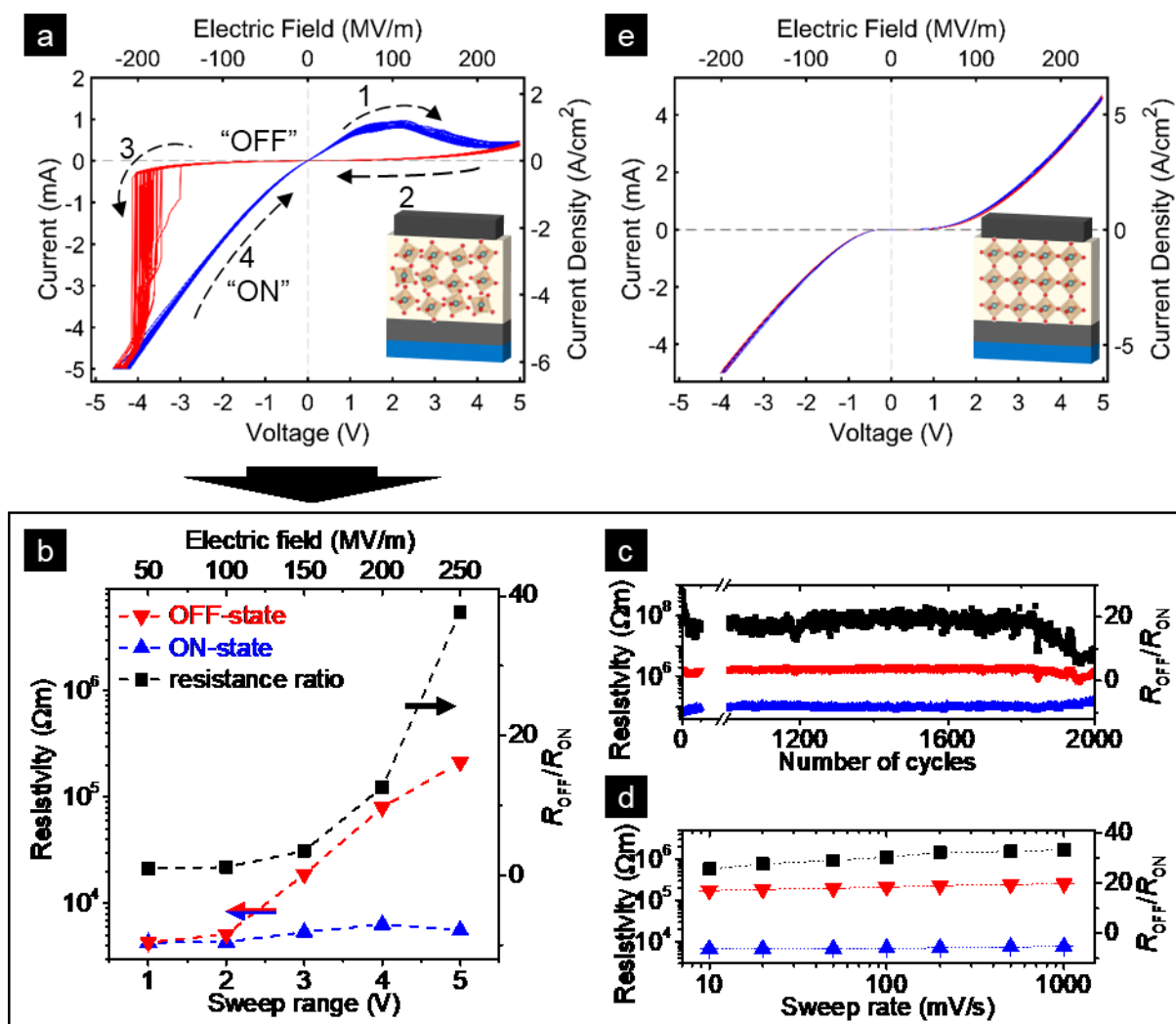
**Figure 2. a)** Exemplary I-V-curve of an amorphous device showing resistive switching for ± 5V. **b)** The appearance of resistive switching in a pristine amorphous device by a subsequent increase of the voltage sweep range. ON-resistance (blue ▲), OFF-resistance (red ▼) and the resistance ratio (black ■) are represented. The lines serve as a guide for the eye. **c)** Stability of an amorphous device cycled at ± 5V. ON-resistance (blue ▲), OFF-resistance (red ▼) and the resistance ratio (black ■) are represented. **d)** Sweep-rate dependence of an amorphous device between 10–1000 mV/s. ON-resistance (blue ▲), OFF-resistance (red ▼) and the resistance ratio (black ■) are represented. **e)** Exemplary I-V-curve of an epitaxial device showing no hysteretic behavior.
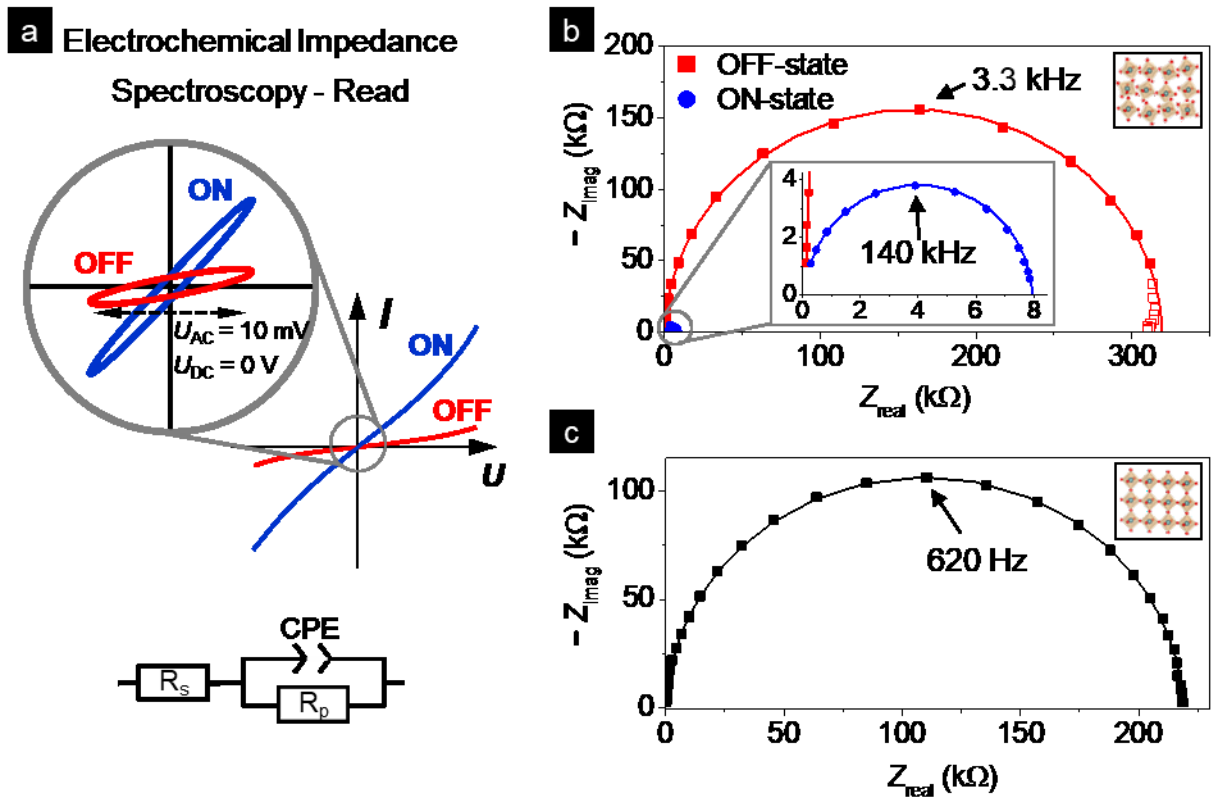
**Figure 3.** a) Schematic representation of electrochemical impedance spectroscopic measurement in ON and OFF-state, adapted from ref.[14]. b) Impedance spectra of both ON- and OFF-state of the amorphous memristive device on a 160µm electrode. c) Impedance spectrum of the crystalline device on a 320 µm electrode.
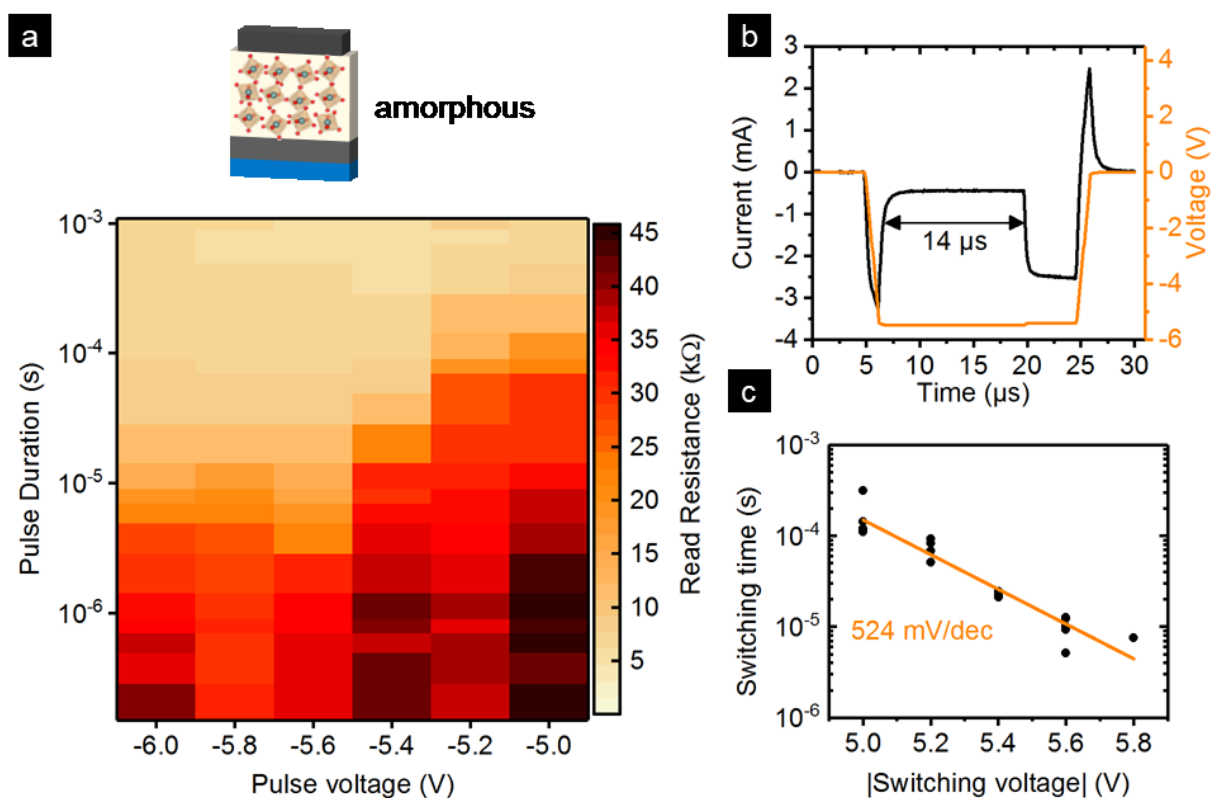
**Figure 4.** Switching SET kinetics of the amorphous $LaFeO_3$ devices under voltage pulses. a) Resistive switching performance map showing the device read-resistance after a SET pulse of a given voltage and time. b) Current transient of a 20 μs-long switching pulse at -5.4 V. c) Switching time versus switching voltage kinetics data highlighting the specific $\Delta V/\Delta \tau_{log}$ slope.
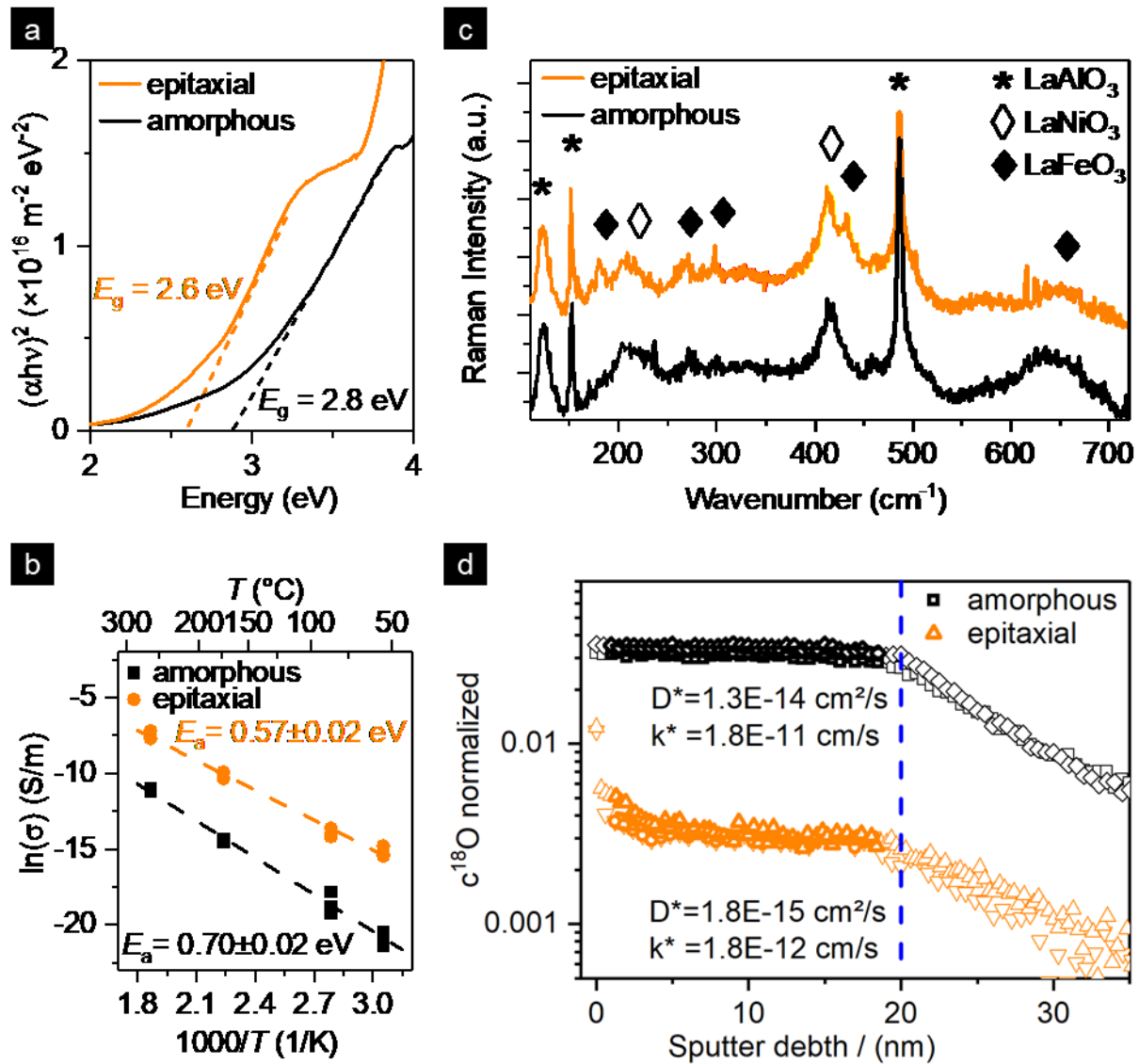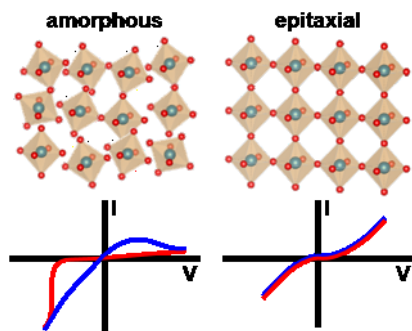
**Figure 5.** a) Tauc plot representation of the linear absorption spectrum of both amorphous (black) and epitaxial (orange) LaFeO$_3$ devices. b) Arrhenius plot of the electrical conductivity showing the impact of the microstructure on the activation energy. c) Raman spectra of the X–ray-amorphous and the epitaxial device. d) $^{18}$O tracer concentration of the amorphous s and epitaxial device after oxygen exchange. The data was normalized to the $^{18}$O concentration in the atmosphere; the blue dotted line represents the bottom LaFeO$_3$ interface.

## Text for Table of Contents (TOC)

The resistive switching performance of model devices based on amorphous or epitaxial LaFeO$_3$ is compared. Only the highly defectuous amorphous systems show reproducible memristance owing to an order of magnitude higher oxygen-ionic diffusion coefficient compared to the epitaxial devices, and not to electronic defect state changes.